AGU ADVANCING EARTH AND SPACE SCIENCES

Geophysical Research Letters

RESEARCH LETTER
10.1029/2024GL112959

Thermobaric Activation of Fault Friction

S. Barbot[1], S. E. Guvercin[1], L. Zhang[2], H. Zhang[1], and Z. Yang[2]

[1]Department of Earth Sciences, University of Southern California, Los Angeles, CA, USA, [2]Institute of Geology, China Earthquake Administration Chaoyang, Beijing, China

Key Points:

- The temperature boundaries of the seismogenic zone depend on confining pressure, implying a thermobaric activation of fault friction
- The model explains schist, granite, gabbro, hornblende, clays, and natural gouge friction evolution with velocity, temperature, and pressure
- The constitutive model provides a realistic representation of fault behavior during seismic cycles applicable to all tectonic contexts

Supporting Information:

Supporting Information may be found in the online version of this article.

Correspondence to:

S. Barbot,
sbarbot@usc.edu

Citation:

Barbot, S., Guvercin, S. E., Zhang, L., Zhang, H., & Yang, Z. (2025). Thermobaric activation of fault friction. *Geophysical Research Letters*, *52*, e2024GL112959. https://doi.org/10.1029/2024GL112959

Received 10 OCT 2024
Accepted 14 FEB 2025

Author Contributions:

Conceptualization: S. Barbot
Data curation: S. Barbot
Formal analysis: S. Barbot
Funding acquisition: S. Barbot
Investigation: S. Barbot, S. E. Guvercin, H. Zhang, Z. Yang
Resources: L. Zhang
Writing – original draft: S. Barbot
Writing – review & editing: S. Barbot, S. E. Guvercin

Abstract The constitutive behavior of faults intervenes in virtually every aspect of the seismic phenomenon but is poorly understood, particularly regarding how effective normal stress affects the boundaries of the seismogenic zone. Here, we explore the mechanical properties of Pelona schist, Westerly granite, phyllosilicate-rich gouge, gabbro, hornblende, lawsonite blueschist, montmorillonite, and smectite in hydrothermal conditions at various confining pressures and explain the laboratory observations with a physical model of fault friction. The thermobaric activation of healing and deformation mechanisms explains the boundaries of unstable slip as a function of slip-rate, temperature, and effective normal stress for a given lithology. The constitutive law affords extrapolation of laboratory data in the conditions relevant to seismic cycles throughout the crust, explaining the focus of large earthquakes in collision, subduction, and continental and oceanic transform settings.

Plain Language Summary An important goal of earthquake physics involves predicting the failure of rocks under the various physical conditions encountered during the seismic cycle. Here, we analyze mechanical data for Pelona schist, Westerly granite, phyllosilicate-rich gouge, gabbro, hornblende, lawsonite blueschist, montmorillonite, and smectite that reveal how normal stress, temperature, and slip-rate affect the frictional properties of rocks. We capture these effects consistently at constant coefficients with a physics-based constitutive friction law. The boundaries of the seismogenic zone follow a thermobaric activation, whereby the transition temperature is a function of pressure. Increasing confining pressure may induce or inhibit velocity-weakening behavior, depending on the constitutive properties controlling the healing and deformation mechanisms. The constitutive model provides an increasingly realistic representation of fault behavior during seismic cycles applicable to a wide range of tectonic contexts.

1. Introduction

The mechanical behavior of faults is inherently complex, producing distinct transient and steady-state responses to small perturbations in normal stress (Linker & Dieterich, 1992; Chen, Niemeijer, & Spiers, 2024; Hong & Marone, 2005), slip-rate (Dieterich, 1979; Lockner & Byerlee, 1986), and temperature (Chester, 1994) with relative magnitudes depending on the ambient physical and kinematic conditions (for example, Blanpied et al., 1995; den Hartog et al., 2021; Mei et al., 2024; Niemeijer et al., 2016; Okuda et al., 2023; Zhang & He, 2016). Characterizing the underlying processes that control fault stability under the conditions found in the brittle crust is key to building increasingly accurate representations of the seismic cycle (for example, Barbot et al., 2012; Barbot, 2020; Gauriau et al., 2023; Julve et al., 2023; Julve et al., 2025; L. Wang and Barbot, 2020; Nie & Barbot, 2021; Sathiakumar et al., 2020, 2024; Shi et al., 2020; B. Wang and Barbot, 2023; B. Wang and Barbot, 2024). The evolution of effective frictional properties with slip-rate, normal stress, pore-fluid pressure, and temperature control the depth extent of the seismogenic zone, the brittle-to-flow transition, and overall fault behavior (for example, Shimamoto, 1986; Noda & Shimamoto, 2010). Extensive laboratory efforts document the evolution of frictional properties with slip-rate and normal stress at room or low temperature (for example, Barth et al., 2013; Collettini et al., 2011; Carpenter et al., 2015; Carpenter et al., 2016; Chen, Affinito, et al., 2024; den Hartog, Peach, et al., 2012; Kaproth & Marone, 2013; Numelin et al., 2007; Noda & Shimamoto, 2009; Zhang & He, 2013; A. R. Niemeijer and Collettini, 2014; Rabinowitz et al., 2018; Scuderi & Collettini, 2016, 2018; Scuderi & Carpenter, 2022). Fewer studies explore the frictional behavior of natural and synthetic gouge in the range of temperatures found deeper in the brittle crust (for example, Blanpied et al., 1995, 1998; Barbot & Zhang, 2023; den Hartog et al., 2023; den Hartog, Niemeijer, & Spiers, 2012; King & Marone, 2012; Lei et al., 2024; Niemeijer et al., 2016; Okuda et al., 2023; Zhang & He, 2016).

Laboratory observations are critical to constraining physical models of fault friction (for example, Aharonov & Scholz, 2018, 2019; Barbot, 2023, 2024a; J. Chen and Spiers, 2016; Mei & Rudnicki, 2023; Mei & Wang, 2024;

Shimamoto & Noda, 2014), with a current focus on the slip-rate and temperature dependence of fault friction (Barbot, 2022, 2023; Nie & Barbot, 2024) and the thermal activation of the brittle-ductile transition (Barbot & Zhang, 2023; Chen et al., 2020; Noda & Shimamoto, 2012). The controlling effect of confining pressure is increasingly well documented but still poorly understood physically (for example, Brace & Byerlee, 1970; Ikari et al., 2009; Kurzawski et al., 2016, 2018; Okuda et al., 2021; Saffer & Marone, 2003, and references therein). An important takeaway is the separate roles of the confining and pore-fluid pressures (Bedford et al., 2021; Okamoto et al., 2020; Xing et al., 2019) that cannot simply be combined into effective normal stress.

In this study, we analyze mechanical data for Pelona schist, Westerly granite (Kilgore et al., 1993), phyllosilicate-rich mylonitic gouge (Zhang & He, 2016), gabbro (He et al., 2007), hornblende (Y. Liu and He, 2020), lawsonite blueschist (Sawai et al., 2016), montmorillonite (Mizutani et al., 2017), and smectite (Saffer & Marone, 2003) that document the thermobaric controls of fault friction for a wide range of temperatures, slip-rates, and normal stress with lithologies relevant to fault zones in various tectonic settings. We present the laboratory data for Pelona schist, hornblende, phyllosilicate, and gabbro gouge in Section 2 and explain the observations with an updated constitutive model in Section 3. Although the laboratory constraints are less comprehensive for lawsonite blueschist (Sawai et al., 2016), montmorillonite (Mizutani et al., 2017), Westerly granite (Kilgore et al., 1993), and smectite (Saffer & Marone, 2003), the model is thoroughly compatible with these observations, as shown in Section 4. The constitutive framework affords extrapolation of laboratory measurements in the range of conditions found in the crust during seismic cycles, capturing the temperature, slip-rate, and pressure controls on the depth of the seismogenic zone in a compact expression with constant parameters. Extrapolation of laboratory data to the in situ conditions of earthquake nucleation explains the focus of the 1971 Mw 6.6 San Fernando, CA, the 2008 Mw 7.9 Wenchuan, China, and the Blanco transform fault Mw 6 earthquakes, demonstrating the relevance of the physical model to the collision, continental transform, and oceanic transform tectonic settings.

2. Laboratory Observations

We consider mechanical datasets for Pelona schist, hornblende, phyllosilicate, and gabbro gouge that exhibit different pressure controls. We first consider a new set of experimental results for Pelona schist gouge. Sample PLS2, a mafic schist composed dominantly of chlorite and amphiboles, originates from Sierra Pelona, California (34.57785°N, 118.37073°W), which exposes Late-Cretaceous, Early Cenozoic underplated sediments from the Farallon plate flat subduction. Due to their origin and current emplacement, the Pelona schists are relevant to understanding the dynamics of subduction megathrusts and the deformation of the lower continental crust in Southern California.

We conduct velocity-step experiments under triaxial, hydrothermal conditions varying the axial loading rate in two repeating sequences involving 1.0, 0.2, and 0.04 μm/s conducted at temperatures from 100°C to 500°C by steps of 100°C and effective normal stress of approximately 100 MPa, 200 MPa, and 300 MPa, including a constant pore-fluid pressure of 30 MPa. More details of the triaxial experimental setup can be found in He et al. (2006). The resulting frictional data (Figure S1 in Supporting Information S1) reveal a complex behavior dictated by the background slip-rate, temperature, and normal stress.

We analyze the frictional response using the RSFit3000 methodology (Skarbek & Savage, 2019) using the slip-rate and state-dependent friction law in isothermal, isobaric conditions (Ruina, 1983), providing the evolution of the direct effect and steady-state velocity dependence parameters

$$a = \frac{\partial \mu}{\partial \ln V}$$
$$a - b = \frac{\partial \mu_{ss}}{\partial \ln V}, \tag{1}$$

where μ and μ_{ss} are the friction coefficient and its steady-state value, respectively, as a function of background slip-rate, temperature, and normal stress. The steady-state parameter is better constrained than the individual values of a and b due to trade-offs caused by finite machine stiffness. A frictional response characterized by $a - b < 0$ is referred to as steady-state velocity weakening, a necessary condition for spontaneous nucleation under isothermal conditions.

The mechanical data reveal three distinct stability regimes characterized by positive and negative steady-state velocity dependence parameters $a - b$ (Figure 1). Steady-state velocity-strengthening occurs at low-temperature, high slip-rate, and low normal stress. The steady-state velocity-weakening domain is confined to intermediate conditions. Another velocity-strengthening domain occurs in high temperature, low slip-rate, and high confining pressure conditions, associated with an increase in the direct effect parameter. As the normal stress increases, the velocity dependence of friction and the temperature range of the velocity-weakening domain decrease (Figure 2). The temperatures and slip-rates bounding the velocity-weakening domain are functions of the confining pressure.

Previously published datasets for hornblende (Y. Liu and He, 2020), gabbro (He et al., 2007), and phyllosilicate-rich gouge (Zhang & He, 2016) deformed in velocity steps from 100°C to 600°C by steps of 100°C at different effective normal stresses provide similar constraints (Figure 3, Figures S7, S8, S10, and S11 in Supporting Information S1). For phyllosilicate and gabbro gouge, we process the raw laboratory data to unravel the slip-rate, temperature, and pressure controls (Figures S6 and S9 in Supporting Information S1). In all cases, the mechanical response can be divided into three stability regimes, whereby steady-state velocity-weakening friction occurs at an intermediate range of temperatures. Increasing slip-rate at low temperatures stabilizes deformation. In contrast, at high temperatures, high slip-rates cause unstable embrittlement. The effect of effective normal stress differs for the various samples. For hornblende, increasing the effective normal stress at high temperatures induces a transition to the velocity-weakening regime (Figure 3). For phyllosilicate and gabbro gouge, increasing the effective normal stress stabilizes deformation (Figures S8 and S11 in Supporting Information S1).

These laboratory observations illustrate different possible controls of the effective normal stress on the dominant deformation and healing mechanisms and the corresponding stability transitions. We seek a physical model that consistently explains these observations at constant coefficients throughout the various slip-rates, temperatures, and pressure experimental conditions.

3. Constitutive Framework With Thermobaric Activation

We describe a constitutive framework that captures the distinct behaviors of rocks under various thermobaric conditions. We assume that the frictional resistance is proportional to the real area of contact that forms at contact junctions (Dieterich & Kilgore, 1994, 1996; Maegawa et al., 2015; Yashima et al., 2015). The area of contact junctions depends on the size of micro-asperities and the effective normal stress, following (Barbot, 2019, 2024a)

$$\mathcal{A} = \frac{\bar{\sigma}}{\chi_n}\left(\frac{d}{d_0}\right)^{\alpha}\left(\frac{\bar{\sigma}}{\sigma_0}\right)^{-\beta}, \tag{2}$$

where $\mathcal{A} = A_r/A_0$ is the real area of contact density, expressed as the ratio of the real area and the nominal area of contact, $\bar{\sigma}$ and $\sigma_0 = 100\text{MPa}$ are the effective normal stress, including the effect of pore-fluid pressure, and a reference value, respectively, χ_n is a proportionality factor commensurate with the indentation hardness (Dieterich & Kilgore, 1994), d and $d_0 = 1\mu\text{m}$ are the size of micro-asperities and a representative value, respectively, and α and β are power-law exponents smaller than unity. The proportionality between real area of contact and frictional resistance is given explicitly by

$$\tau_y = \mathcal{A}\chi, \tag{3}$$

where χ is a material property comparable to the plowing hardness. The frictional resistance can be obtained in non-isothermal, non-isobaric conditions as (Barbot, 2023)

$$\frac{V}{V_0} = \sum_{k=1}^{M}\left(\frac{\tau}{\tau_y}\right)^{n_k}\exp\left[-\frac{Q_k}{R}\left(\frac{1}{T}-\frac{1}{\bar{T}_k}\right)\right], \tag{4}$$

which incorporates the stress power-law exponent n_k, the activation energy Q_k, and the activation temperature $\bar{T}_k$ for M brittle or semi-brittle deformation mechanisms. The deformation mechanism associated with the lowest power exponent n_k is considered semi-brittle. The parameters V_0, d_0, and σ_0 in Equations 2 and 4 indicate the choice of physical unit or the order of magnitude for the respective dynamic parameters. For simplicity,

10.1029/2024GL112959

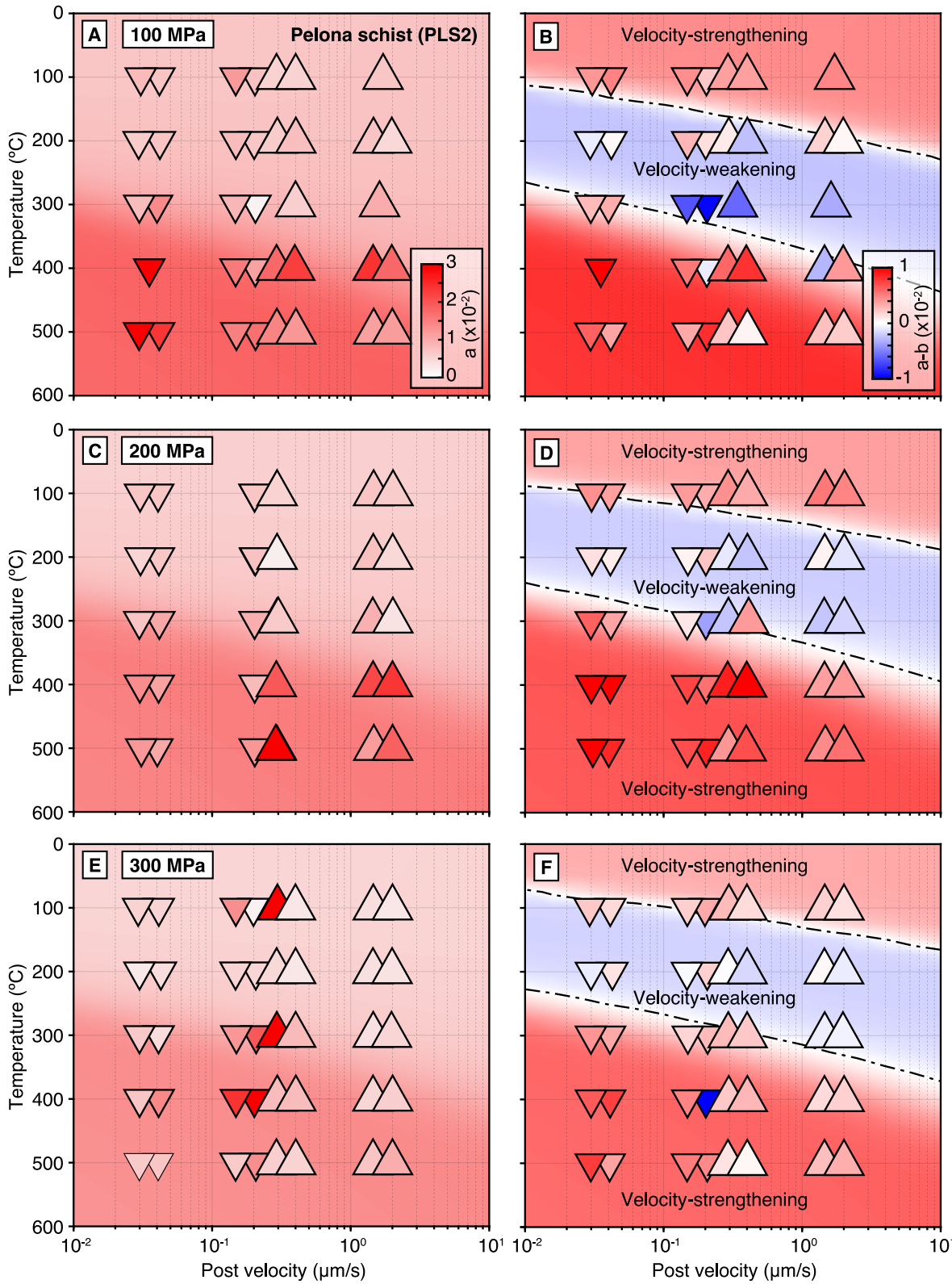

Figure 1. Frictional properties of Pelona schist (PLS2) as a function of temperature and slip-rate in a triaxial, hydrothermal setting for various effective normal stress. (a), (b) Direct effect and steady-state parameters a and $a - b$, respectively at 100 MPa confining pressure, (c), (d) Same at 200 MPa confining pressure, and (e), (f) Same at 300 MPa. The laboratory data is shown in upright and downward triangles for up and down velocity steps, respectively, and the prediction of the constitutive model in Section 3 with the parameters in Table S1 in Supporting Information S1 is shown with the background color.

10.1029/2024GL112959

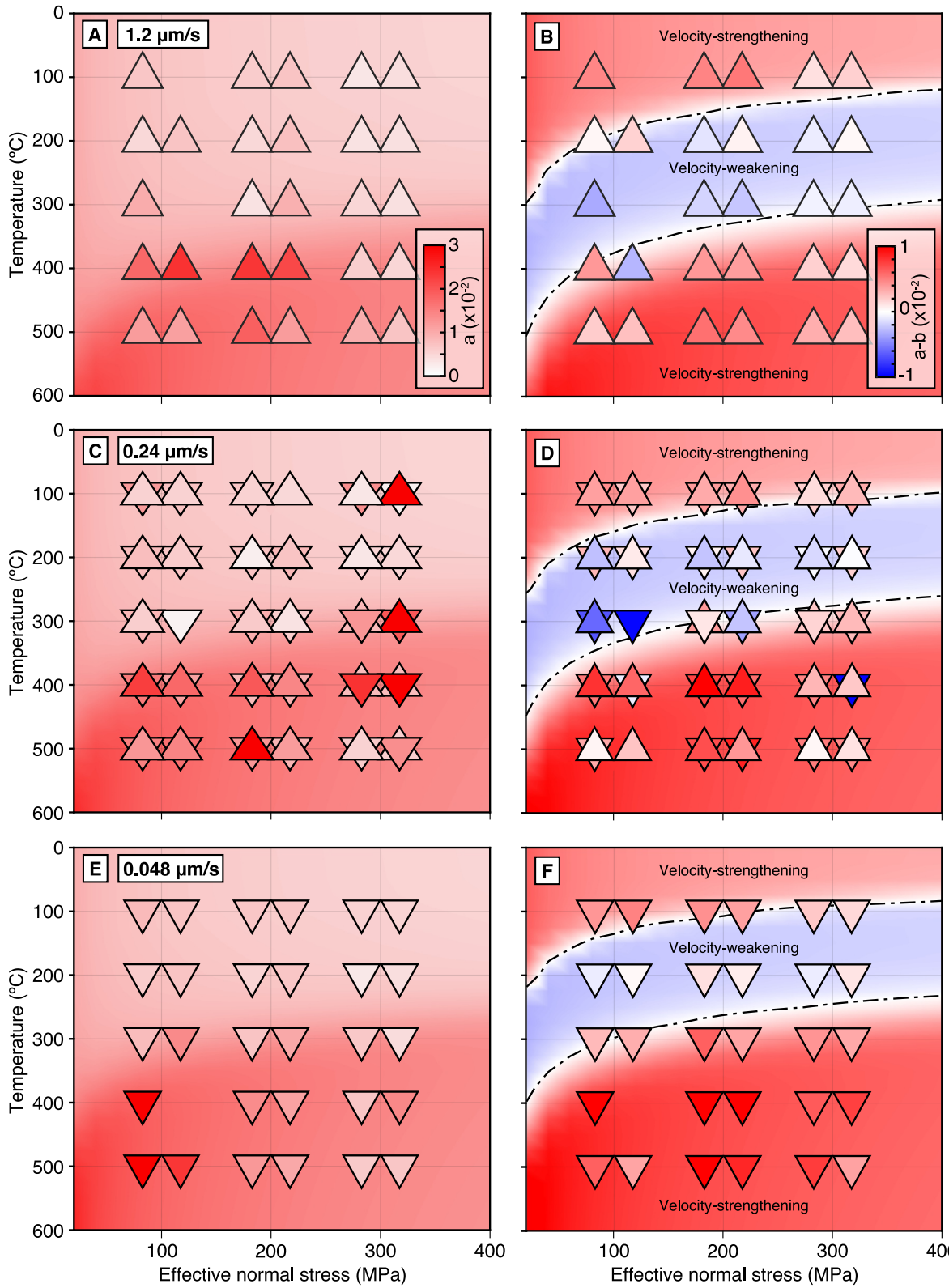

Figure 2. Frictional properties of Pelona schist (PLS2) as a function of temperature and effective normal stress in a triaxial, hydrothermal setting at various slip-rates. (a), (b) Direct effect and steady-state parameters a and $a - b$, respectively at 1.2 μm/s, (c), (d) Same at 0.24 μm/s, and (e), (f) Same at 0.048 μm/s. The laboratory data is shown in upright triangles and the prediction of the constitutive model in Section 3 with the parameters in Table S1 in Supporting Information S1 is shown with the background color.

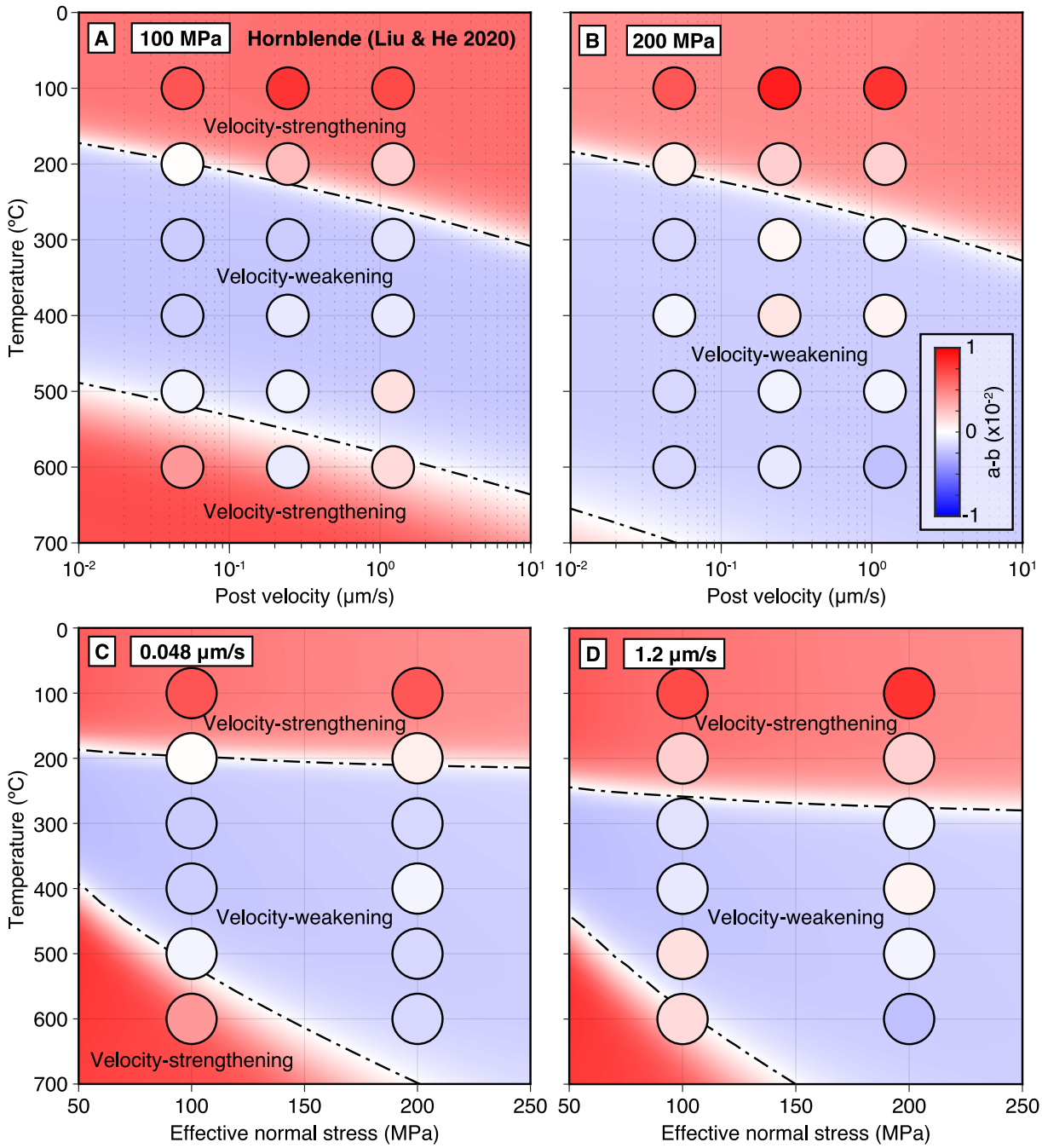

Figure 3. Thermobaric control on the frictional properties of hornblende. (a), (b) Kinematic and thermal control on steady-state velocity dependence parameter $a - b$ at 100 and 200 MPa effective normal stress, respectively, and (c), (d) Thermobaric control of $a - b$ at 0.048 µm/s and 1.2 µm/s, respectively. Inference from laboratory data is shown with colored circles and the model prediction with the background color. The constitutive properties are shown in Table S1 in Supporting Information S1.

Equation 4 does not encompass ductile deformation, which is described elsewhere (Barbot, 2023; Barbot & Zhang, 2023; Barbot, 2024b). The thermobaric activation is obtained by prescribing the pressure dependence of the activation temperature as follows

$$\frac{1}{\bar{T}_k} = \frac{1}{T_k^0} - \frac{\zeta_k R}{Q_k} \ln \frac{\bar{\sigma}}{\sigma_0}, \tag{5}$$

where ζ_k is the compressibility factor of a non-ideal gas, as described in Appendix A. Combining Equations 2–5, we obtain the slip-rate-, temperature-, and normal-stress-dependent constitutive law

$$\frac{V}{V_0} = \sum_{k=1}^{M} \left(\frac{\tau}{\mu_0 \bar{\sigma}}\right)^{n_k} \left(\frac{d}{d_0}\right)^{-\alpha n_k} \left(\frac{\bar{\sigma}}{\sigma_0}\right)^{\beta n_k - \zeta_k} \exp\left[-\frac{Q_k}{R}\left(\frac{1}{T} - \frac{1}{T_k^0}\right)\right], \tag{6}$$

where each term of the product describes the control of the respective dynamic variable for a given deformation mechanism k, and we introduced the reference friction coefficient $\mu_0 = \chi/\chi_n$.

The size of micro-asperities evolves due to plastic deformation around contact junctions and the random rejuvenation of contacts during fault slip (Barbot, 2019). Normal stress drives the thermally activated creep at contact junctions leading to gouge compaction (Barbot, 2024a). The evolution law that governs the size of micro-asperities can be cast as the aging-law end-member, given by (Barbot, 2024b)

$$\frac{\dot{d}}{d} = \sum_{k=1}^{N} \frac{G_k}{p_k d^{p_k}} \left(\frac{\bar{\sigma}}{\sigma_0}\right)^{q_k} \exp\left[-\frac{H_k}{R}\left(\frac{1}{T} - \frac{1}{T_k}\right)\right] - \frac{\lambda V}{2h}, \tag{7}$$

involving N healing mechanisms associated with the reference growth coefficient $G_k = 1\mu m^{p_k}/s$, the activation energy H_k, the activation temperature T_k, and the asperity-size power exponent p_k and the normal stress power exponent q_k, where h is the gouge layer thickness and $1/\lambda$ is a characteristic strain for contact rejuvenation, or the slip-law end-member (Barbot, 2024b)

$$\frac{\dot{d}}{d} = \frac{\lambda V}{2h} \ln\left\{\frac{2h}{\lambda V} \sum_{k=1}^{N} \frac{G_k}{p_k d^{p_k}} \left(\frac{\bar{\sigma}}{\sigma_0}\right)^{q_k} \exp\left[-\frac{H_k}{R}\left(\frac{1}{T} - \frac{1}{T_k}\right)\right]\right\}. \tag{8}$$

The potential effect of a thermobaric activation of healing involving a compressibility factor is readily incorporated in the power exponent q_k. Equations 7 and 8 produce the same micro-asperity size at steady state. Together, Equations 6 and 7 or Equations 6 and 8 explain the frictional behavior of rocks for a wide range of physical conditions, including the direct and transient response to temperature steps (Barbot, 2019, 2024b), normal stress steps (Barbot, 2024a), and velocity steps across the brittle-to-flow transition at various background slip-rates and temperatures (Barbot & Zhang, 2023; Barbot, 2022, 2023, 2024b).

We compare the model predictions of the frictional parameters with the laboratory observations. Although not included explicitly in the formulation, the direct and steady-state velocity-dependence parameters can be obtained using Equation 1, allowing direct comparison with typical laboratory data (Figures 1–3, Figures S7, S8, S10, and S11 in Supporting Information S1). We obtain the best-fitting parameters using a grid search (Figure S2 in Supporting Information S1). The constitutive parameters can be constrained well considering the mechanical data at all slip-rates, temperatures, and pressures simultaneously (Figure S3 in Supporting Information S1). Some residuals remain due to the unaccounted dependence of the frictional properties with total strain and tradeoffs arising during parameter estimation. The laboratory measurements can be explained consistently using constant parameters by invoking $M = 2$ brittle deformation mechanisms and $N = 2$ healing mechanisms with the constitutive parameters shown in Table S1 in Supporting Information S1.

The competition of healing mechanisms explains the low-temperature transition from steady-state velocity-strengthening friction to velocity-weakening friction as a function of temperature, slip-rate, and effective normal stress for Pelona schist, hornblende, gabbro, and phyllosilicate-rich gouge. For Pelona schist, the transition temperature decreases with increasing normal stress. The slope of the low-temperature stability transition in the pressure-temperature space is controlled by the difference in the ratios q_k/p_k of the two healing mechanisms (Figure S4 in Supporting Information S1). For hornblende, the slope is slightly positive.

The constitutive model captures the stability transition at high temperatures for Pelona schist, hornblende, and phyllosilicate gouge, even though they feature different slopes in pressure-temperature space, with a negative slope for Pelona schist and phyllosilicate-rich gouge and a positive slope for hornblende. Semi-brittle deformation occurs at lower effective normal stress than brittle deformation at high temperatures, illustrating that semi-brittle deformation may not always be the intermediate behavior between the brittle and ductile regimes. The slope of the

high-temperature stability transition in pressure-temperature space is controlled by the ratios ζ_k/n_k (Figure S5 in Supporting Information S1). A negative slope is obtained when the low-temperature deformation mechanism is more dilatant than the high-temperature deformation mechanism. As a deformation mechanism may be more dilatant than the other, positive or negative transition slopes in pressure-temperature space are possible (Figures S4 and S5 in Supporting Information S1).

4. Discussion

Our analysis of new and published laboratory experiments demonstrates the non-stationarity of frictional properties, which evolve gradually within a narrow range of physical conditions, but change abruptly with significant deviations in normal stress, slip-rate, or temperature.

For Pelona schist, gabbro, and phyllosilicate-rich gouge, increasing the effective normal stress tends to lower the temperature boundaries of the velocity-weakening domain and decrease the velocity dependence of friction. In contrast, increasing normal stress widens the temperature range of the velocity-weakening domain of hornblende. The frictional properties of other rocks showcase intermediate behaviors. This is illustrated by the mechanical data from rotary shear experiments on lawsonite blueschist gouge (Sawai et al., 2016) at effective normal stress ranging from 25 to 200 MPa with equal pore-fluid pressure at temperatures from 22°C to 400°C (Figure 4a). For lawsonite blueschist, increasing effective normal stress shrinks the temperature range of the velocity-weakening domain. The constitutive model captures this behavior well, although the effect of varying pore fluid pressure is not included. The constitutive framework also explains the triaxial experiments on montmorillonite gouge (Mizutani et al., 2017) from 10 to 70 MPa effective normal stress including a constant pore-fluid pressure of 10 MPa (Figure 4b). For montmorillonite, increasing pressure widens the temperature range of the velocity-weakening domain. The constitutive model also explains the barometric and kinematic dependence of frictional properties of Westerly granite (Kilgore et al., 1993) and smectite (Saffer & Marone, 2003) in double-direct shear at room temperature (Figures 4c and 4d). The constitutive parameters are shown in Tables S1 and S2 in Supporting Information S1.

The proposed thermobaric activation of fault friction may be compatible with several other laboratory experiments conducted at low temperatures. The steady-state parameter $a - b$ increases with normal stress for foliated gouge (sample "2f") from the Zuccale Fault, Italy, associated with a progressive loss of sensitivity to normal stress at high slip velocity (Collettini et al., 2011). Talc-calcite mixtures experience an increase of $a - b$ with normal stress (Giorgetti et al., 2015). Brucite gouge transitions from velocity weakening to velocity strengthening with increasing normal stress at room temperature (Okuda et al., 2021). The above observations may all manifest a transition of healing mechanism. An opposing view attributes the change of velocity dependence and stability to the enhanced localization induced by confining pressure (Kurzawski et al., 2016). However, their laboratory observations on hemipelagic clay and calcareous ooze can also be explained by the thermobaric activation of competing healing mechanisms with $q_1/p_1 > q_2/p_2$.

The constitutive law provides a novel framework to elucidate key aspects of seismogenesis across various tectonic settings by linking laboratory-measured frictional properties with seismic observations (Figure 5). The frictional properties of Pelona schist, which underplates much of Southern California (Chapman, 2017), may explain the depth of local seismicity (Magistrale & Zhou, 1996). Assuming a geothermal gradient of 20°C/km (Shinevar et al., 2018), over-pressurized fluids within the fault zone corresponding to an effective normal stress of 30 MPa, and slip-rates of 0.2 nm/s representative of nucleation, Pelona schist PLS2 is steady-state velocity-weakening up to 14 km depth, coinciding with the maximum depth of coseismic slip for the 1971 Mw 6.6 San Fernando, CA earthquake. Likewise, the phyllosilicate-rich mylonitic gouge collected from the Wenchuan-Maoxian fault (Zhang & He, 2016) is compatible with the depth distribution of coseismic slip of the 2008 Mw 7.9 Wenchuan, China earthquake, assuming a geothermal gradient of 20°C/km (Zhu et al., 2016). Finally, the frictional properties of gabbro explain the depth distribution of the Mw 6 earthquakes at the Blanco transform fault, where they focus between 3 and 6 km depth within the oceanic crust (Kuna et al., 2019), due to the high geothermal gradient of 50-60°C/km characteristic of a young oceanic plate (Liu et al., 2022). Hence, extrapolating the frictional behavior of rocks outside laboratory conditions is key to improving physical models of seismicity.

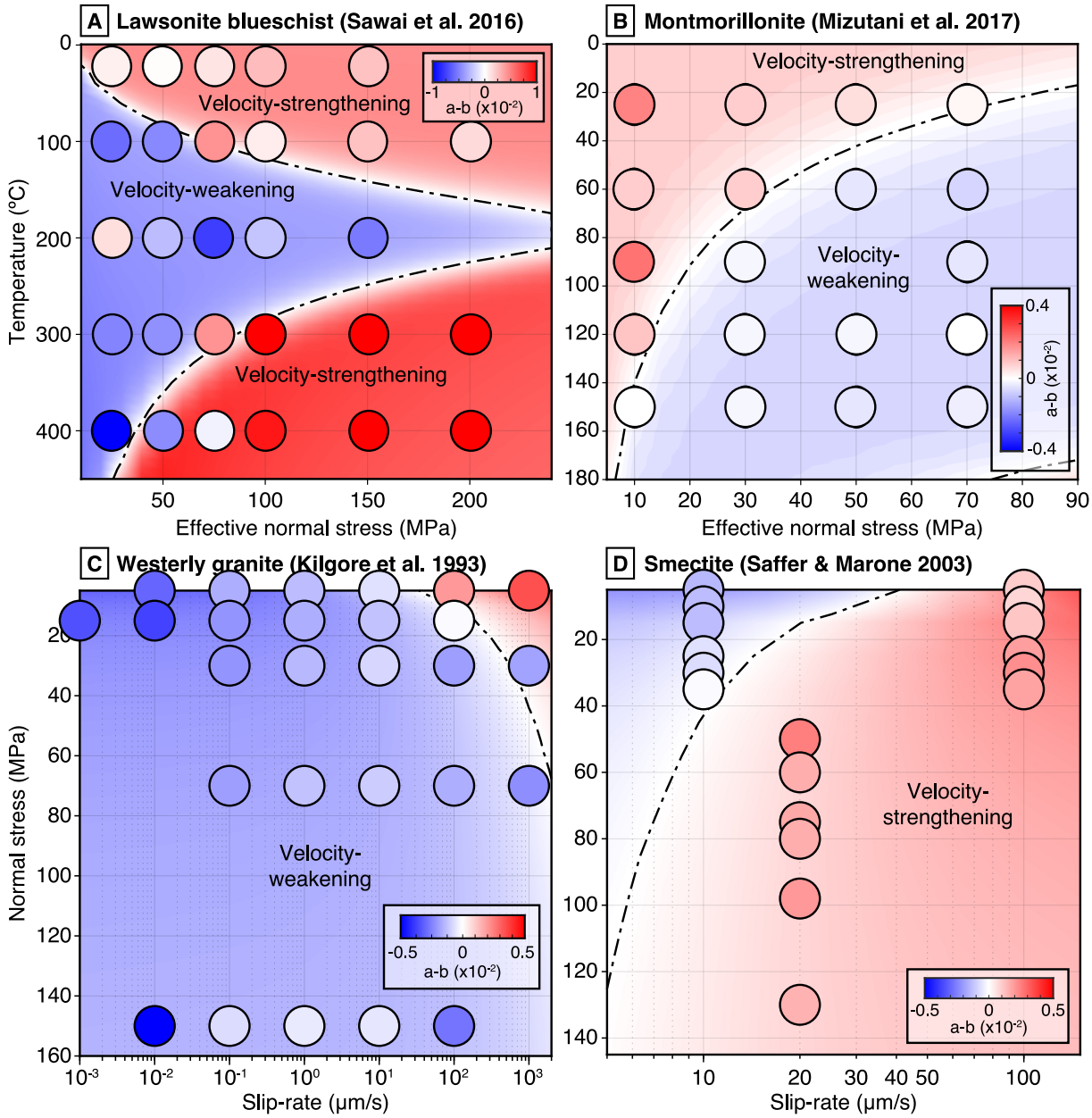

Figure 4. Thermobaric and kinematic control on the frictional properties of (a) lawsonite blueschist (Sawai et al., 2016), (b) montmorillonite (Mizutani et al., 2017), (c) Westerly granite (Kilgore et al., 1993), and (d) smectite (Saffer & Marone, 2003). The colored circles indicate inference from laboratory observations and the background color indicates the model prediction. The constitutive properties are shown in Tables S1 and S2 in Supporting Information S1.

5. Conclusions

The complex constitutive behavior of rocks upon failure is tractable, at least regarding the effects of temperature, slip-rate, and effective normal stress for a given lithology. The friction coefficient inherits a dependence on normal stress from the real area of contact and the thermobaric activation of deformation, with opposite effects. The thermobaric activation of fault friction implies varying amplitudes of dilatancy for different deformation mechanisms, making the temperature boundaries of the seismogenic zone dependent on confining pressure.

Integrating the effects of slip-rate, temperature, and effective normal stress in the constitutive framework is paramount in estimating the frictional behavior in natural conditions. The frictional properties of Pelona schist, phyllosilicate-rich natural gouge, and gabbro are compatible with the focal depths of the 1971 Mw 6.6 San

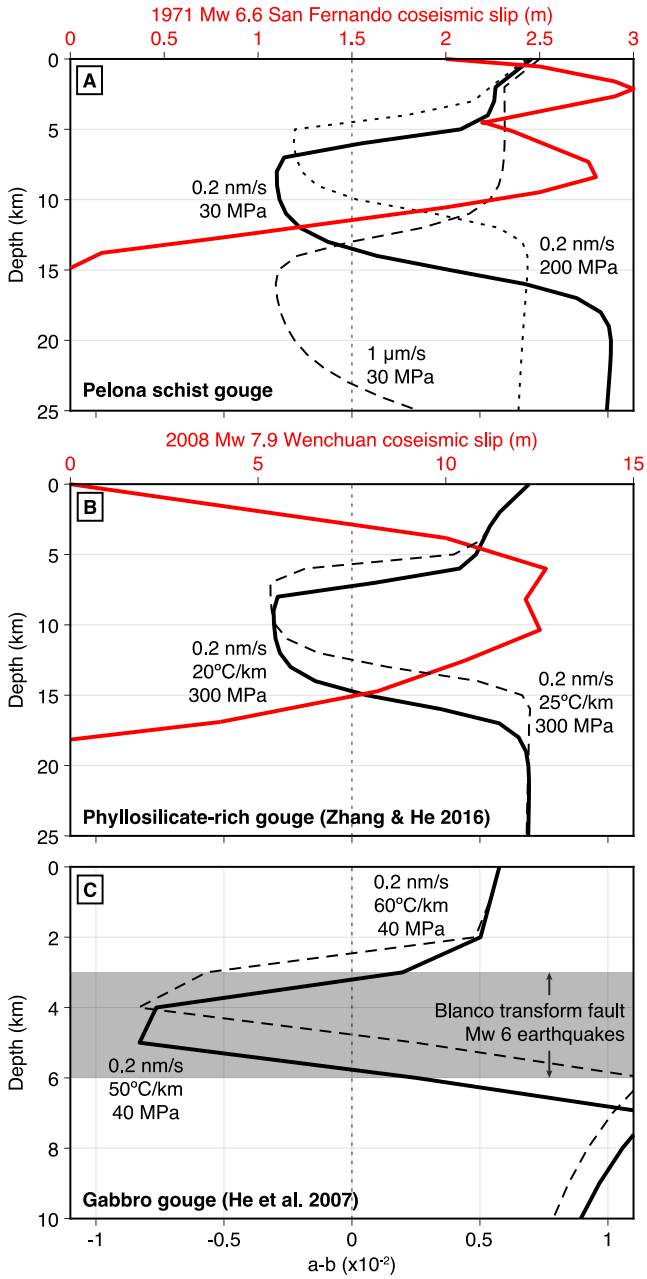

Figure 5. Thermobaric control on the depth of the seismogenic zone and coseismic slip. (a) Comparison between the slip distribution of the 1971 Mw 6.6 San Fernando, CA earthquake (Heaton, 1982) and the frictional properties of Pelona schist (PLS2), (b) Comparison between the slip distribution of the 2008 Mw 7.9 Wenchuan, China earthquake (Fielding et al., 2013) and the frictional properties of phyllosilicate-rich gouge collected in the Sichuan Basin (Zhang & He, 2016), and (c) Comparison between the depth distribution of Mw 6 earthquakes along the Blanco transform fault (Kuna et al., 2019) and the frictional properties of gabbro (He et al., 2007), representative of the oceanic crust. The physical model allows extrapolation of the laboratory data at slip-rates of 0.2 nm/s, representative of earthquake nucleation.

Fernando, 2008 Mw 7.8 Wenchuan, and Mw 6 earthquakes on the Blanco transform fault, respectively, considering slip-rate relevant to earthquake nucleation. Hence, the constitutive framework affords the means to reconcile seismic activity with local lithology in realistic in situ conditions. With broad applicability for rocks of various metamorphic grades found in subduction zones, continental and oceanic crusts, and natural fault zones, the constitutive model provides an important link connecting rock mechanics and fault dynamics.

Appendix A: Thermodynamics of Brittle and Semi-Brittle Deformation

Plastic deformation of fault gouge in the brittle and semi-brittle regimes can be considered as a transformation of the form

$$A \xrightarrow{\Delta G} B,$$

where A is the reference state of matter of a representative volume element for a mole of the gouge constituents and B is the thermodynamically irreversible deformed state (for example, Gibbs, 1969). We assume that each state can be described individually by the corresponding molar Gibbs free energies G_A and G_B. The change of Gibbs free energy $\Delta G = G_B - G_A$ across the transition from state A to state B describes the spontaneity of the transition, with $\Delta G < 0$ corresponding to a spontaneous transition, $\Delta G = 0$ corresponding to equilibrium, and $\Delta G > 0$ indicating that the transformation is not spontaneous.

The kinetics of transformation can be described by absolute rate theory (Eyring, 1936), with a thermal activation of the rate of transformation. The frequency of successful deformation increments follows

$$f = \Psi_0 \frac{k_B T}{\hbar} \exp\left[-\frac{\Delta G}{RT}\right], \tag{A1}$$

where Ψ_0 is a unitless scaling factor, k_B is Boltzmann's constant, $\hbar$ is Planck's constant, R is the universal gas constant, and T is the absolute temperature. As the transformation represents plastic deformation, slip-rate is proportional to the frequency of successful deformation increments. We assume that the slip distance produced by deformation increments is a power-law of shear stress. Accordingly, we write

$$V = \lambda_0 \left(\frac{\tau}{\tau_y}\right)^n f, \tag{A2}$$

where λ_0 is a characteristic slip distance, τ is the norm of the traction vector across a frictional interface, and τ_y is the yield strength given by Equation 3. Combining Equations A1 and A2, we obtain the constitutive relationship

$$V = V_0 \left(\frac{\tau}{\tau_y}\right)^n \exp\left(-\frac{\Delta G}{RT}\right), \tag{A3}$$

where we have defined $V_0 = \lambda_0 \Psi_0 k_B T/\hbar$. Given the exponential function of temperature, the linear temperature dependence of V_0 can be neglected at first order. Equation A3 is of the form of Equation 4 in the main text, explaining the functional form of the constitutive framework. The remaining step is to characterize the change of Gibbs free energy for plastic deformation.

Within each state, the Gibbs free energy is defined as

$$G = H - TS, \tag{A4}$$

where H is the enthalpy of the state under consideration and S is the entropy of a representative volume V_Ω of the mechanical system Ω. As the Gibbs free energy is continuous within each state, the total derivative follows the standard thermodynamic relationship

$$dG = V_\Omega\, dP - SdT. \tag{A5}$$

However, the state transition involves a change of heat capacity and atomic configuration. As a result, the enthalpy and entropy of the system change, leading to a discontinuity in Gibbs free energy across the transition, described by

$$\Delta G = \Delta H - T\Delta S, \tag{A6}$$

where $\Delta H = H_B - H_A$ and $\Delta S = S_B - S_A$.

We are interested in the slope of the transition in pressure-temperature space, that is, the Clapeyron slope of the transformation. On each side of the equilibrium, Equation A5 holds. Furthermore, as $\Delta G = 0$ is constant along the transition line, we have $dG = 0$. Hence, along the equilibrium line, we can write

$$\frac{dP}{dT} = \frac{\Delta S}{\Delta V}, \tag{A7}$$

where $\Delta V = V_B - V_A$ is the molar change of volume of the constituents, starting from a representative volume element. By definition, we have $\Delta G = \Delta H - T\Delta S = 0$ at equilibrium, so we also get

$$\Delta S = \frac{\Delta H}{T}. \tag{A8}$$

Combining Equations A7 and A8, we obtain the Clapeyron slope for plastic deformation in pressure-temperature space

$$\frac{dP}{dT} = \frac{1}{T}\frac{\Delta H}{\Delta V}, \tag{A9}$$

where P and T refer to the pressure and temperature anywhere along the equilibrium line.

An equation of state is needed to relate the change of volume ΔV to the ambient temperature and pressure conditions. We approximate the change of volume by the volume of the deformed state

$$\Delta V = V_B - V_A \approx V_B, \tag{A10}$$

compatible with experimental evidence for volume change during shear (Marone et al., 1990; Proctor et al., 2020; Samuelson et al., 2009). Finally, we describe the deformed state by a non-ideal gas law for a molar volume of a solid-state solution, as follows

$$V_B = \frac{\zeta RT}{P}, \tag{A11}$$

where ζ is the compressibility factor. Combining Equations A9, A10, and (A11), we obtain the Clapeyron slope of plastic deformation

$$\frac{dP}{dT} = \frac{P}{T^2}\frac{\Delta H}{\zeta R}. \tag{A12}$$

Integrating Equation A12 on both sides, we find

$$P = P_0 \exp\left[-\frac{\Delta H}{\zeta R}\left(\frac{1}{T} - \frac{1}{T_0}\right)\right], \tag{A13}$$

where P_0 and T_0 are constants of integration, or, equivalently,

$$\frac{1}{T} = \frac{1}{T_0} - \frac{\zeta R}{\Delta H} \ln \frac{P}{P_0}, \tag{A14}$$

which corresponds to Equation 5 in the main text with a slight change of nomenclature. The change of Gibbs free energy becomes

$$\Delta G = T\ \Delta H\left(\frac{1}{T} - \frac{1}{T_0} + \frac{\zeta R}{\Delta H} \ln \frac{P}{P_0}\right). \tag{A15}$$

Combining Equations A3 and A15, we obtain

$$V = V_0\left(\frac{\tau}{\tau_y}\right)^n \left(\frac{P}{P_0}\right)^{-\zeta} \exp\left[-\frac{\Delta H}{R}\left(\frac{1}{T} - \frac{1}{T_0}\right)\right]. \tag{A16}$$

For simplification, we approximate the pressure by the effective normal stress, and we equate the activation energy to the change of enthalpy, explaining the thermobaric activation of fault friction described in Equation 6 in the main text.

Conflict of Interest

The authors declare no conflicts of interest relevant to this study.

Data Availability Statement

The data and scripts used in this study are available at a zenodo.org repository (Barbot, 2025).

Acknowledgments
The manuscript benefited from the constructive comments of the Associate Editor, Dr. Cheng Mei, and an anonymous reviewer. We are grateful for the technical support of Prof. Changrong He at the Institute of Geology, China Earthquake Administration. The study is funded by the National Science Foundation under award number EAR-1848192 and by the National Natural Science Foundation of China under Grant 42274234.

References

Aharonov, E., & Scholz, C. H. (2018). A physics-based rock friction constitutive law: Steady state friction. *Journal of Geophysical Research*, *123*(2), 1591–1614. https://doi.org/10.1002/2016JB013829

Aharonov, E., & Scholz, C. H. (2019). The brittle-ductile transition predicted by a physics-based friction law. *Journal of Geophysical Research*, *124*(3), 2721–2737. https://doi.org/10.1029/2018JB016878

Barbot, S. (2019). Modulation of fault strength during the seismic cycle by grain-size evolution around contact junctions. *Tectonophysics*, *765*, 129–145. https://doi.org/10.1016/j.tecto.2019.05.004

Barbot, S. (2020). Frictional and structural controls of seismic super-cycles at the Japan trench. *Earth Planets and Space*, *72*(63), 63. https://doi.org/10.1186/s40623-020-01185-3

Barbot, S. (2022). A rate-state-and temperature-dependent friction law with competing healing mechanisms. *Journal of Geophysical Research*, *127*(11), e2022JB025106. https://doi.org/10.1029/2022JB025106

Barbot, S. (2023). Constitutive behavior of rocks during the seismic cycle. *AGU Advances*, *4*(5). https://doi.org/10.1029/2023AV000972

Barbot, S. (2024a). Transient and steady-state friction in non-isobaric conditions. *Geochemistry, Geophysics, Geosystems*, *25*(2), e2023GC011279. https://doi.org/10.1029/2023GC011279

Barbot, S. (2024b). Does the direct effect of friction increase continuously with absolute temperature? *Proceedings of the National Academy of Sciences*, *121*(42). https://doi.org/10.1073/pnas.2405111121

Barbot, S. (2025). Thermobaric activation of fault friction [Dataset]. *Zenodo*. https://doi.org/10.5281/zenodo.14873299

Barbot, S., Lapusta, N., & Avouac, J. P. (2012). Under the hood of the earthquake machine: Towards predictive modeling of the seismic cycle. *Science*, *336*(6082), 707–710. https://doi.org/10.1126/science.1218796

Barbot, S., & Zhang, L. (2023). Constitutive behavior of olivine gouge across the brittle-ductile transition. *Geophysical Research Letters*, *50*(24). https://doi.org/10.1029/2023GL105916

Barth, N., Boulton, C., Carpenter, B., Batt, G., & Toy, V. (2013). Slip localization on the southern alpine fault, New Zealand. *Tectonics*, *32*(3), 620–640. https://doi.org/10.1002/tect.20041

Bedford, J. D., Faulkner, D. R., Allen, M. J., & Hirose, T. (2021). The stabilizing effect of high pore-fluid pressure along subduction megathrust faults: Evidence from friction experiments on accretionary sediments from the Nankai Trough. *Earth and Planetary Science Letters*, *574*, 117161. https://doi.org/10.1016/j.epsl.2021.117161

Blanpied, M., Marone, C., Lockner, D., Byerlee, J., & King, D. (1998). Quantitative measure of the variation in fault rheology due to fluid-rock interactions. *Journal of Geophysical Research*, *103*(B5), 9691–9712. https://doi.org/10.1029/98JB00162

Blanpied, M. L., Lockner, D. A., & Byerlee, J. D. (1995). Frictional slip of granite at hydrothermal conditions. *Journal of Geophysical Research*, *100*(B7), 13045–13064. https://doi.org/10.1029/95JB00862

Brace, W., & Byerlee, J. (1970). California earthquakes: Why only shallow focus? *Science*, *168*(3939), 1573–1575. https://doi.org/10.1126/science.168.3939.15

Carpenter, B., Ikari, M., & Marone, C. (2016). Laboratory observations of time-dependent frictional strengthening and stress relaxation in natural and synthetic fault gouges. *Journal of Geophysical Research*, *121*(2), 1183–1201. https://doi.org/10.1002/2015jb012136

Carpenter, B., Saffer, D., & Marone, C. (2015). Frictional properties of the active San Andreas Fault at SAFOD: Implications for fault strength and slip behavior. *Journal of Geophysical Research*, *120*(7), 5273–5289. https://doi.org/10.1002/2015JB011963

Chapman, A. D. (2017). The pelona–orocopia–rand and related schists of southern California: A review of the best-known archive of shallow subduction on the planet. *International Geology Review*, *59*(5–6), 664–701. https://doi.org/10.1080/00206814.2016.1230836

Chen, J., Niemeijer, A. R., & Spiers, C. J. (2024). Rapid normal stress oscillations cause weakening and anelastic dilation in gouge-bearing faults. *Geophysical Research Letters*, *51*(15), e2024GL109755. https://doi.org/10.1029/2024GL109755

Chen, J., & Spiers, C. J. (2016). Rate and state frictional and healing behavior of carbonate fault gouge explained using microphysical model. *Journal of Geophysical Research*, *121*(12), 8642–8665. https://doi.org/10.1002/2016jb013470

Chen, K., Avouac, J.-P., Aati, S., Milliner, C., Zheng, F., & Shi, C. (2020). Cascading and pulse-like ruptures during the 2019 ridgecrest earthquakes in the eastern California shear zone. *Nature Communications*, *11*(1), 1–8. https://doi.org/10.1038/s41467-019-13750-w

Chen, T.-W., Affinito, R., Marone, C., Fisher, D., Smye, A., & Hashimoto, Y. (2024). Frictional properties and healing behavior of tectonic mélanges: Implications for the evolution of subduction fault zones. *Journal of Geophysical Research*, *129*(6), e2023JB028472. https://doi.org/10.1029/2023JB028472

Chester, F. M. (1994). Effects of temperature on friction: Constitutive equations and experiments with fault gouge. *Journal of Geophysical Research*, *99*(B4), 7247–7261. https://doi.org/10.1029/93JB03110

Collettini, C., Niemeijer, A., Viti, C., Smith, S. A., & Marone, C. (2011). Fault structure, frictional properties and mixed-mode fault slip behavior. *Earth and Planetary Science Letters*, *311*(3), 316–327. https://doi.org/10.1016/j.epsl.2011.09.020

den Hartog, S., Marone, C., & Saffer, D. (2023). Frictional behavior downdip along the subduction megathrust: Insights from laboratory experiments on exhumed samples at in situ conditions. *Journal of Geophysical Research*, *128*(1), e2022JB024435. https://doi.org/10.1029/2022JB024435

den Hartog, S., Niemeijer, A., & Spiers, C. J. (2012). New constraints on megathrust slip stability under subduction zone P–T conditions. *Earth and Planetary Science Letters*, *353*, 240–252. https://doi.org/10.1016/j.epsl.2012.08.022

den Hartog, S., Thomas, M. Y., & Faulkner, D. (2021). How do laboratory friction parameters compare with observed fault slip and geodetically derived friction parameters? Insights from the longitudinal valley fault, Taiwan. *Journal of Geophysical Research*, *126*(10), e2021JB022390. https://doi.org/10.1029/2021JB022390

den Hartog, S. A., Peach, C. J., de Winter, D. M., Spiers, C. J., & Shimamoto, T. (2012). Frictional properties of megathrust fault gouges at low sliding velocities: New data on effects of normal stress and temperature. *Journal of Structural Geology*, *38*, 156–171. https://doi.org/10.1016/j.jsg.2011.12.001

Dieterich, J. H. (1979). Modeling of rock friction 1. experimental results and constitutive equations. *Journal of Geophysical Research*, *84*(B5), 2161–2168. https://doi.org/10.1029/JB084iB05p02161

Dieterich, J. H., & Kilgore, B. D. (1994). Direct observation of frictional contacts: New insights for sliding memory effects. *Pure and Applied Geophysics*, *143*(1–3), 283–302. https://doi.org/10.1007/BF00874332

Dieterich, J. H., & Kilgore, B. D. (1996). Imaging surface contacts: Power law contact distributions and contact stresses in quartz, calcite, glass and acrylic plastic. *Tectonophysics*, *256*(1–4), 219–239. https://doi.org/10.1016/0040-1951(95)00165-4

Eyring, H. (1936). Viscosity, plasticity, and diffusion as examples of absolute reaction rates. *Journal of Chemical Physics*, *4*(4), 283–291. https://doi.org/10.1063/1.1749836

Fielding, E. J., Sladen, A., Li, Z., Avouac, J.-P., Bürgmann, R., & Ryder, I. (2013). Kinematic fault slip evolution source models of the 2008 M7. 9 Wenchuan earthquake in China from SAR interferometry, GPS and teleseismic analysis and implications for Longmen Shan tectonics. *Geophysical Journal International*, *194*(2), 1138–1166. https://doi.org/10.1093/gji/ggt155

Gauriau, J., Barbot, S., & Dolan, J. F. (2023). Islands of chaos in a sea of periodic earthquakes. *Earth and Planetary Science Letters*, *618*, 118274. https://doi.org/10.1016/j.epsl.2023.118274

Gibbs, G. (1969). Thermodynamic analysis of dislocation glide controlled by dispersed local obstacles. *Materials Science and Engineering*, *4*(6), 313–328. https://doi.org/10.1016/0025-5416(69)90026-3

Giorgetti, C., Carpenter, B., & Collettini, C. (2015). Frictional behavior of talc-calcite mixtures. *Journal of Geophysical Research*, *120*(9), 6614–6633. https://doi.org/10.1002/2015JB011970

He, C., Wang, Z., & Yao, W. (2007). Frictional sliding of gabbro gouge under hydrothermal conditions. *Tectonophysics*, *445*(3–4), 353–362. https://doi.org/10.1016/j.tecto.2007.09.008

He, C., Yao, W., Wang, Z., & Zhou, Y. (2006). Strength and stability of frictional sliding of gabbro gouge at elevated temperatures. *Tectonophysics*, *427*(1–4), 217–229. https://doi.org/10.1016/j.tecto.2006.05.023

Heaton, T. H. (1982). The 1971 San Fernando earthquake: A double event? *Bulletin of the Seismological Society of America*, *72*(6A), 2037–2062. https://doi.org/10.1785/BSSA07206A2037

Hong, T., & Marone, C. (2005). Effects of normal stress perturbations on the frictional properties of simulated faults. *Geochemistry, Geophysics, Geosystems*, *6*(3). https://doi.org/10.1029/2004GC000821

Ikari, M. J., Saffer, D. M., & Marone, C. (2009). Frictional and hydrologic properties of clay-rich fault gouge. *Journal of Geophysical Research*, *114*(B5). https://doi.org/10.1029/2008jb006089

Julve, J., Barbot, S., Moreno, M., Tassara, A., Araya, R., Catalán, N., et al. (2023). Recurrence time and size of Chilean earthquakes influenced by geological structure. *Nature Geoscience*, *17*, 1–9. https://doi.org/10.1038/s41561-023-01327-8

Julve, J., Moreno, M., Barbot, S., & Tassara, A. (2025). Impact of upper-plate faulting on megathrust foreshocks: Insights from the 2014 iquique earthquake. *Geophysical Research Letters*, *52*(3), e2024GL111064. https://doi.org/10.1029/2024GL111064

Kaproth, B. M., & Marone, C. (2013). Slow earthquakes, preseismic velocity changes, and the origin of slow frictional stick-slip. *Science*, *341*(6151), 1229–1232. https://doi.org/10.1126/science.1239577

Kilgore, B. D., Blanpied, M. L., & Dieterich, J. H. (1993). Velocity dependent friction of granite over a wide range of conditions. *Geophysical Research Letters*, *20*(10), 903–906. https://doi.org/10.1029/93GL00368

King, D., & Marone, C. (2012). Frictional properties of olivine at high temperature with applications to the strength and dynamics of the oceanic lithosphere. *Journal of Geophysical Research*, *117*(B12). https://doi.org/10.1029/2012JB009511

Kuna, V. M., Nábělek, J. L., & Braunmiller, J. (2019). Mode of slip and crust–mantle interaction at oceanic transform faults. *Nature Geoscience*, *12*(2), 138–142. https://doi.org/10.1038/s41561-018-0287-1

Kurzawski, R. M., Niemeijer, A. R., Stipp, M., Charpentier, D., Behrmann, J. H., & Spiers, C. J. (2018). Frictional properties of subduction input sediments at an erosive convergent continental margin and related controls on décollement slip modes: The Costa Rica Seismogenesis Project. *Journal of Geophysical Research*, *123*(10), 8385–8408. https://doi.org/10.1029/2017JB015398

Kurzawski, R. M., Stipp, M., Niemeijer, A. R., Spiers, C. J., & Behrmann, J. H. (2016). Earthquake nucleation in weak subducted carbonates. *Nature Geoscience*, *9*(9), 717–722. https://doi.org/10.1038/ngeo2774

Lei, H., Niemeijer, A. R., Zhou, Y., & Spiers, C. J. (2024). Frictional properties of natural granite fault gouge under hydrothermal conditions: A case study of strike-slip fault from Anninghe fault zone, southeastern Tibetan plateau. *Journal of Geophysical Research*, *129*(8), e2024JB028760. https://doi.org/10.1029/2024JB028760

Linker, M. H., & Dieterich, J. H. (1992). Effects of variable normal stress on rock friction: Observations and constitutive relations. *Journal of Geophysical Research*, *97*(B4), 4923–4940. https://doi.org/10.1029/92JB00017

Liu, M., Gerya, T., & Rozel, A. B. (2022). Self-organization of magma supply controls crustal thickness variation and tectonic pattern along melt-poor mid-ocean ridges. *Earth and Planetary Science Letters*, *584*, 117482. https://doi.org/10.1016/j.epsl.2022.117482

Liu, Y., & He, C. (2020). Friction properties of hornblende and implications for slow-slip events in subduction zones. *Tectonophysics*, *796*, 228644. https://doi.org/10.1016/j.tecto.2020.228644

Lockner, D., & Byerlee, J. (1986). Laboratory measurements of velocity-dependent frictional strength*, no. 86-147 in Open File Report*. U.S. Geological Survey. https://doi.org/10.3133/ofr86417

Maegawa, S., Itoigawa, F., & Nakamura, T. (2015). Effect of normal load on friction coefficient for sliding contact between rough rubber surface and rigid smooth plane. *Tribology International*, *92*, 335–343. https://doi.org/10.1016/j.triboint.2015.07.014

Magistrale, H., & Zhou, H.-w. (1996). Lithologic control of the depth of earthquakes in southern California. *Science*, *273*(5275), 639–642. https://doi.org/10.1126/science.273.5275.639

Marone, C., Raleigh, B. C., & Scholz, C. H. (1990). Frictional behavior and constitutive modeling of simulated fault gouge. *Journal of Geophysical Research*, *95*(B5), 7007–7026. https://doi.org/10.1029/JB095iB05p07007

Mei, C., Mercuri, M., & Rudnicki, J. W. (2024). Rock friction experiments and modeling under hydrothermal conditions. *Earth-Science Reviews*, *254*, 104824. https://doi.org/10.1016/j.earscirev.2024.104824

Mei, C., & Rudnicki, J. W. (2023). Microphysical modeling of fault slip and stability transition in hydrothermal conditions. *Geophysical Research Letters*, *50*(13), e2023GL103730. https://doi.org/10.1029/2023GL103730

Mei, C., & Wang, L. (2024). Velocity dependence of rate-and-state friction in granular fault gouge and implications for slow-slip events. *Journal of Geophysical Research*, *129*(7), e2024JB029393. https://doi.org/10.1029/2024JB029393

Mizutani, T., Hirauchi, K.-i., Lin, W., & Sawai, M. (2017). Depth dependence of the frictional behavior of montmorillonite fault gouge: Implications for seismicity along a décollement zone. *Geophysical Research Letters*, *44*(11), 5383–5390. https://doi.org/10.1002/2017GL073465

Nie, S., & Barbot, S. (2021). Seismogenic and tremorgenic slow slip near the stability transition of frictional sliding. *Earth and Planetary Science Letters*, *569*, 117037. https://doi.org/10.1016/j.epsl.2021.117037

Nie, S., & Barbot, S. (2024). Velocity and temperature dependence of steady-state friction of natural gouge controlled by competing healing mechanisms. *Geophysical Research Letters*, *51*(11), e2023GL106485. https://doi.org/10.1029/2023GL106485

Niemeijer, A., Boulton, C., Toy, V., Townend, J., & Sutherland, R. (2016). Large-displacement, hydrothermal frictional properties of DFDP-1 fault rocks, Alpine Fault, New Zealand: Implications for deep rupture propagation. *Journal of Geophysical Research*, *121*(2), 624–647. https://doi.org/10.1002/2015JB012593

Niemeijer, A. R., & Collettini, C. (2014). Frictional properties of a low-angle normal fault under in situ conditions: Thermally-activated velocity weakening. *Pure and Applied Geophysics*, *171*(10), 2641–2664. https://doi.org/10.1007/s00024-013-0759-6

Noda, H., & Shimamoto, T. (2009). Constitutive properties of clayey fault gouge from the Hanaore fault zone, southwest Japan. *Journal of Geophysical Research*, *114*(B4). https://doi.org/10.1029/2008JB005683

Noda, H., & Shimamoto, T. (2010). A rate- and state-dependent ductile flow law of polycrystalline halite under large shear strain and implications for transition to brittle deformation. *Geophysical Research Letters*, *37*(L09310). https://doi.org/10.1029/2010GL042512

Noda, H., & Shimamoto, T. (2012). Transient behavior and stability analyses of halite shear zones with an empirical rate-and-state friction to flow law. *Journal of Structural Geology*, *38*, 234–242. https://doi.org/10.1016/j.jsg.2011.08.012

Numelin, T., Marone, C., & Kirby, E. (2007). Frictional properties of natural fault gouge from a low-angle normal fault, Panamint Valley, California. *Tectonics*, *26*(2). https://doi.org/10.1029/2005TC001916

Okamoto, A. S., Niemeijer, A. R., Takeshita, T., Verberne, B. A., & Spiers, C. J. (2020). Frictional properties of actinolite-chlorite gouge at hydrothermal conditions. *Tectonophysics*, *779*, 228377. https://doi.org/10.1016/j.tecto.2020.228377

Okuda, H., Katayama, I., Sakuma, H., & Kawai, K. (2021). Effect of normal stress on the frictional behavior of brucite: Application to slow earthquakes at the subduction plate interface in the mantle wedge. *Solid Earth*, *12*(1), 171–186. https://doi.org/10.5194/se-12-171-2021

Okuda, H., Niemeijer, A. R., Takahashi, M., Yamaguchi, A., & Spiers, C. J. (2023). Hydrothermal friction experiments on simulated basaltic fault gouge and implications for megathrust earthquakes. *Journal of Geophysical Research*, *128*(1), e2022JB025072. https://doi.org/10.1029/2022JB025072

Proctor, B., Lockner, D., Kilgore, B., Mitchell, T., & Beeler, N. (2020). Direct evidence for fluid pressure, dilatancy, and compaction affecting slip in isolated faults. *Geophysical Research Letters*, *47*(16), e2019GL086767. https://doi.org/10.1029/2019GL086767

Rabinowitz, H., Savage, H., Skarbek, R., Ikari, M. J., Carpenter, B. M., & Collettini, C. (2018). Frictional behavior of input sediments to the Hikurangi Trench, New Zealand. *Geochemistry, Geophysics, Geosystems*, *19*(9), 2973–2990. https://doi.org/10.1029/2018GC007633

Ruina, A. (1983). Slip instability and state variable friction laws. *Journal of Geophysical Research*, *88*(B12), 10359–10370. https://doi.org/10.1029/JB088iB12p10359

Saffer, D. M., & Marone, C. (2003). Comparison of smectite-and illite-rich gouge frictional properties: Application to the updip limit of the seismogenic zone along subduction megathrusts. *Earth and Planetary Science Letters*, *215*(1–2), 219–235. https://doi.org/10.1016/S0012-821X(03)00424-2

Samuelson, J., Elsworth, D., & Marone, C. (2009). Shear-induced dilatancy of fluid-saturated faults: Experiment and theory. *Journal of Geophysical Research*, *114*(B12). https://doi.org/10.1029/2008JB006273

Sathiakumar, S., Barbot, S., & Hubbard, J. (2020). Seismic cycles in fault-bend folds. *Journal of Geophysical Research*, *125*(8), e2019JB018557. https://doi.org/10.1029/2019JB018557

Sathiakumar, S., Barbot, S., & Hubbard, J. (2024). The role of fault structural evolution on long-term slip rates and seismic cycles in the Himalayan orogenic wedge. *Earth and Planetary Science Letters*, *630*, 118599. https://doi.org/10.1016/j.epsl.2024.118599

Sawai, M., Niemeijer, A. R., Plümper, O., Hirose, T., & Spiers, C. J. (2016). Nucleation of frictional instability caused by fluid pressurization in subducted blueschist. *Geophysical Research Letters*, *43*(6), 2543–2551. https://doi.org/10.1002/2015GL0675

Scuderi, M. M., & Carpenter, B. M. (2022). Frictional stability and hydromechanical coupling of serpentinite-bearing fault gouge. *Geophysical Journal International*, *231*(1), 290–305. https://doi.org/10.1093/gji/ggac188

Scuderi, M. M., & Collettini, C. (2016). The role of fluid pressure in induced vs. triggered seismicity: Insights from rock deformation experiments on carbonates. *Scientific Reports*, *6*(1), 1–9. https://doi.org/10.1038/srep24852

Scuderi, M. M., & Collettini, C. (2018). Fluid injection and the mechanics of frictional stability of shale-bearing faults. *Journal of Geophysical Research*, *123*(10), 8364–8384. https://doi.org/10.1029/2018JB016084

Shi, Q., Barbot, S., Shibazaki, B., Matsuzawa, T., Wei, S., & Tapponnier, P. (2020). Structural control and system-level behavior of the seismic cycle at the Nankai trough. *Earth Planets and Space*, *72*(1), 1–31. https://doi.org/10.1186/s40623-020-1145-0

Shimamoto, T. (1986). Transition between frictional slip and ductile flow for halite shear zones at room temperature. *Science*, *231*(4739), 711–714. https://doi.org/10.1126/science.231.4739.71

Shimamoto, T., & Noda, H. (2014). A friction to flow constitutive law and its application to a 2-d modeling of earthquakes. *Journal of Geophysical Research*, *119*(11), 8089–8106. https://doi.org/10.1002/2014jb011170

Shinevar, W. J., Behn, M. D., Hirth, G., & Jagoutz, O. (2018). Inferring crustal viscosity from seismic velocity: Application to the lower crust of Southern California. *Earth and Planetary Science Letters*, *494*, 83–91. https://doi.org/10.1016/j.epsl.2018.04.055

Skarbek, R. M., & Savage, H. M. (2019). RSFit3000: A MATLAB GUI-based program for determining rate and state frictional parameters from experimental data. *Geosphere*, *15*(5), 1665–1676. https://doi.org/10.1130/GES02122.1

Wang, B., & Barbot, S. (2023). Pulse-like ruptures, seismic swarms, and tremorgenic slow-slip events with thermally activated friction. *Earth and Planetary Science Letters*, *603*, 117983. https://doi.org/10.1016/j.epsl.2022.117983

Wang, B., & Barbot, S. (2024). Rupture segmentation on the East Anatolian fault (Turkey) controlled by along-strike variations in long-term slip rates in a structurally complex fault system. *Geology*, *52*(10), 779–783. https://doi.org/10.1130/G52403.1

Wang, L., & Barbot, S. (2020). Excitation of San Andreas tremors by thermal instabilities below the seismogenic zone. *Science Advances*, *6*(36), eabb2057. https://doi.org/10.1126/sciadv.abb2057

Xing, T., Zhu, W., French, M., & Belzer, B. (2019). Stabilizing effect of high pore fluid pressure on slip behaviors of gouge-bearing faults. *Journal of Geophysical Research*, *124*(9), 9526–9545. https://doi.org/10.1029/2019JB018002

Yashima, S., Romero, V., Wandersman, E., Frétigny, C., Chaudhury, M., Chateauminois, A., & Prevost, A. (2015). Normal contact and friction of rubber with model randomly rough surfaces. *Soft Matter*, *11*(5), 871–881. https://doi.org/10.1039/C4SM02346C

Zhang, L., & He, C. (2013). Frictional properties of natural gouges from Longmenshan fault zone ruptured during the Wenchuan Mw7. 9 earthquake. *Tectonophysics*, *594*, 149–164. https://doi.org/10.1016/j.tecto.2013.03.030

Zhang, L., & He, C. (2016). Frictional properties of phyllosilicate-rich mylonite and conditions for the brittle-ductile transition. *Journal of Geophysical Research*, *121*(4), 3017–3047. https://doi.org/10.1002/2015JB012489

Zhu, C., Hu, S., Qiu, N., Rao, S., & Yuan, Y. (2016). The thermal history of the Sichuan Basin, SW China: Evidence from the deep boreholes. *Science China Earth Sciences*, *59*(1), 70–82. https://doi.org/10.1007/s11430-015-5116-4